International Journal of Environmental Science and Technology (2026) 23:478
https://doi.org/10.1007/s13762-026-07304-z

ORIGINAL PAPER

Sorption behavior of diclofenac on a kaolinite–biochar composite: adsorption mechanisms and environmental implications

R. Lafi[1] · R. Elleuch[2] · S. Jebri[3] · W. Mabrouk[1] · A. Y. A. Alzahrani[4] · Y. O. Al-Ghamdi[5] · S. M. A. S. Keshk[6]

Received: 3 January 2026 / Revised: 19 April 2026 / Accepted: 19 May 2026

Abstract

Diclofenac sodium (DCF), a common pharmaceutical contaminant, poses risks to both environmental and human health even at low concentrations. Although environmental levels typically fall within the ng/L–µg/L range, this study investigates DCF sorption in the low-mg/L domain (1–10 mg/L) to elucidate adsorption mechanisms and thermodynamic behavior. A kaolinite-biochar composite made from almond shell biomass (Kaol-ASB) was evaluated as a sustainable adsorbent. Electrostatic attraction, hydrogen bonding, and π-π interactions were found to be the most important processes for DCF uptake. The Langmuir model predicted a theoretical monolayer capacity of 125 mg/g, whereas the experimentally observed capacity was approximately 7.5 mg/g. Kinetic and isotherm modeling revealed pseudo-second-order chemisorption and Langmuir-type monolayer binding, with thermodynamic characteristics indicating a spontaneous, slightly endothermic process. Overall, the findings emphasize the importance of interfacial charge modulation in pharmaceutical adsorption and illustrate the potential of kaolinite-biochar composites as ecologically friendly sorbents for reducing pharmaceutical pollution in aquatic systems.

Keywords Clay/biochar composite · Diclofenac removal · Ecological remediation · Adsorption mechanism

Introduction

Pharmaceuticals have received increasing attention due to their persistence in aquatic environments, bioactivity at low concentrations, and continuous input from wastewater effluents. Diclofenac (DCF) is commonly detected in surface water, groundwater, and even treated effluents at levels ranging from nanograms to a few micrograms per liter (Alkan et al. 2007; Khasawneh et al., 2021; Lin et al. 2023). DCF levels in surface waters can range from a few ng/L to several µg/L, depending on proximity to wastewater discharge stations (Khasawneh and Palaniandy 2021; Rodayan et al. 2016). Wastewater treatment plant effluents often contain diclofenac in the low-µg/L range due to inadequate removal during conventional treatment processes (Rivera-Utrilla et al. 2013; Trivedi et al. 2025). Although its environmental concentrations are low, DCF exhibits high ecotoxicological potential, including endocrine disruption, cytotoxicity, and chronic toxicity in aquatic organisms (Kümmerer 2009; Rodayan et al. 2016; Song et al. 2024).

Environmental DCF concentrations typically fall within the ng/L to low-µg/L range; however, the present study employed 1–10 mg/L to enable mechanistic interpretation rather than simulation of trace-level conditions. The resistance of DCF to conventional wastewater treatment processes and its bioaccumulation tendency underscore the need for advanced remediation strategies capable of addressing low-concentration scenarios. The physicochemical properties of DCF compound the challenge of removing it at trace

Editorial responsibility: Samareh Mirkia.

✉ S. M. A. S. Keshk
sherif.keshk@become.institute

[1] Laboratory Water, Membrane and Environmental Biotechnology, CERTE, BP 273, 8020 Borj Cedria, Soliman, Tunisia

[2] Institut Des Molécules Et Matériaux du Mans (IMMM-UMR CNRS 6283), Université du Mans, Avenue Olivier Messiaen, 72085 Le Mans, CEDEX 9, France

[3] Laboratory of Desalination and Valorization of Natural Water, CERTE, BP 273, 8020 Borj Cedria, Soliman, Tunisia

[4] Department of Chemistry, Faculty of Science, King Khalid University, 61413 Abha, Saudi Arabia

[5] Department of Chemistry, College of Science Al-Zulfi, Majmaah University, 11952 Al-Majmaah, Saudi Arabia

[6] Become: Technology, Science, AI and Automation Laboratory, 63 Rue de Tolbiac, 75013 Paris, France

Published online: 01 June 2026

levels; however, the mechanisms investigated here were evaluated at mg/L concentrations rather than true trace-level conditions. With a pKa of approximately 4.48 and a log Kow of 4.51, DCF exists predominantly in its anionic form at environmental pH values (Fig. S3), which reduces its affinity for many conventional adsorbents (Du et al. 2024). Moreover, adsorbents facilitating π–π interactions, hydrogen bonding, and electrostatic attraction are demanded due to their aromatic structure and hydrophobicity. These requirements have driven extensive studies into adsorption-based removal methods that are simple, cost-effective, and scalable compared to advanced oxidation, membrane filtration, or electrochemical treatments (Rivera-Utrilla et al. 2013; Larous et al., 2016; Zubair et al. 2023). Carbonaceous materials, such as activated carbon, biochar, and carbon nanotubes, have been widely studied for DCF adsorption. Activated carbon is the benchmark due to its high surface area and pore structure, yet its widespread application is restricted due to its cost and regeneration limitations (Jodeh et al. 2016). Biochar, which is derived from agricultural waste using pyrolysis, has gained attention as a sustainable alternative. Studies using rice husk, sawdust, and almond shell biochar (ASB) have demonstrated moderate DCF adsorption capacities, typically in the 20–80 mg/g range at concentrations exceeding 50 mg/L (Filipinas et al. 2021; Seymen et al. 2025). However, biochar has suboptimal performance at low DCF concentrations due to limited surface functionality and insufficient interaction sites. To overcome these limitations, composite materials integrating biochar with clays, metal oxides, or surfactants were explored. Clay minerals such as montmorillonite and bentonite possess high cation-exchange capacity and strong surface reactivity, while kaolinite contributes structural stability and surface hydroxyl groups that enhance hybrid adsorbent performance (Alkan et al. 2007; Faghihian et al., 2009). Kaolinite is a 1:1 aluminosilicate clay mineral composed of alternating Si–O and Al–OH layers. Its surface carries pH-dependent charges and provides hydroxyl groups capable of hydrogen bonding and electrostatic interactions (Faghihian et al., 2009). Kaolinite has been used in several pharmaceutical adsorption studies due to its structural stability and moderate cation-exchange capacity, but its performance is limited by low surface area.

Combining kaolinite with biochar can therefore enhance adsorption by integrating mineral surface functionality with carbonaceous porosity. While several clay–biochar composites have been reported, their mechanistic behavior at low mg/L concentrations remains insufficiently resolved, particularly regarding charge-modulated interactions and diffusion-controlled uptake. For instance, kaolinite-modified biochars have shown improved adsorption of antibiotics and dyes through enhanced surface charge and functional-group availability (Yang et al. 2018). However, few studies have applied such composites for DCF removal, and even fewer have examined environmentally relevant concentrations below 10 mg/L (Sharma et al. 2024; Wang et al., 2025). Recent studies explored surfactant-modified biosorbents, such as guava seeds treated with cetyltrimethylammonium bromide (CTAB), which could adsorb up to 38 mg/g of DCF at 45 °C (Coria-Zamudio et al. 2025). These systems are promising, but they often suffer from poor regenerability and limited scalability. Similarly, composites incorporating iron oxides or layered double hydroxides (LDHs) have demonstrated high adsorption capacities, but they have hindered practical deployment due to complex synthesis routes and elevated costs (Silveira et al. 2020). Consequently, a low-cost, regenerable, and mechanistically optimized adsorbent tailored for low-concentration DCF remediation does not exist. Although ecotoxicological impacts occur at µg/L levels, the present study focuses on low-mg/L concentrations to enable mechanistic, kinetic, and thermodynamic evaluation using UV–Vis detection. Validation at true trace levels (µg/L) will require future testing using HPLC-MS or LC-MS/MS. To address this gap, this study proposes a novel kaolinite-modified almond shell biochar (Kaol-ASB) composite specifically designed for efficient removal of DCF at environmentally relevant concentrations (≤ 10 mg/L). The composite, derived from agricultural and mineral waste, is engineered to enhance surface charge modulation and interaction site diversity, enabling effective DCF elimination under low-concentration conditions. The composite incorporates surface charge modulation, pore accessibility, and a variety of interaction sites, outperforming typical biochars and approaching the performance of advanced materials in emerging contaminant removal.The methodology and analytical approach used in this study are in line with published benchmarks that emphasize uncertainty analysis, repeatability, and mechanistic clarity in adsorption-based removal of emerging pollutants (Rocha-Santos et al. 2022; Hernandez-Maldonado et al. 2022). This study is one of the first to assess kaolinite-biochar hybrids for diclofenac removal in the low mg/L range, offering mechanistic insight into adsorption behavior at concentrations below 10 mg/L. The composite improves electrostatic and hydrogen-bonding interactions through interfacial charge manipulation, supported by kinetic, isotherm, and thermodynamic models.

This substance, derived from agricultural and mineral waste, is regenerable and scalable. While the composite demonstrated strong adsorption performance in the low-mg/L range, its effectiveness at environmentally relevant µg/L concentrations remains to be validated in future studies using high-sensitivity analytical techniques such as HPLC-MS or LC-MS/MS (Zubair et al. 2023). The composite may offer future potential for integration into ecological engineering systems such as constructed wetlands and biofilters; however, such applications would require pilot-scale validation to confirm performance under realistic hydraulic

and environmental conditions. Despite extensive research on carbonaceous and mineral-based adsorbents, no study has systematically evaluated a kaolinite–biochar composite for diclofenac removal at low mg/L concentrations using kinetic, isotherm, thermodynamic, and diffusion analyses to establish a coherent mechanistic framework.Recent studies on biochar, clay–carbon hybrids, and advanced composite adsorbents for pharmaceutical removal highlight the need for materials that can operate efficiently at low concentrations while remaining scalable and regenerable (Filipinas et al. 2021; Seymen et al. 2025; Coria-Zamudio et al. 2025; Sharma et al. 2024; Du et al. 2024; Silveira et al. 2020; Fraiha et al. 2024; Hernandez-Maldonado et al., 2022; Rocha-Santos et al., 2022). This dual emphasis on mechanistic clarity and ecological application defines the novelty of the work. The central hypothesis posited that the synergistic integration of kaolinite into the biochar matrix would combine the high porosity and π–π interaction potential of biochar with the surface-charge modulation and hydrogen bonding capabilities of kaolinite to enhance adsorption performance. This synergy was expected to facilitate multilayer adsorption, pore-filling, and strong adsorbate–adsorbent interactions under realistic pH and concentration conditions. To evaluate this hypothesis, the composite was synthesized using controlled pyrolysis and mineral integration, followed by comprehensive physicochemical characterizations using Fourier transform infrared spectroscopy (FTIR), X-ray diffraction (XRD), scanning electron microscopy (SEM), and zeta potential analysis. Adsorption experiments at low DCF concentrations simulated real-world contamination scenarios. Kinetic modeling, equilibrium isotherm fitting (Langmuir and Freundlich), and thermodynamic analysis supported the mechanistic interpretation. Furthermore, intraparticle diffusion (IPD) and speciation modeling elucidated transport dynamics and interaction pathways.

Materials and methods

Chemicals, materials, and instruments

This study used analytical grade reagents procured from Sigma-Aldrich. A stock DCF solution was prepared by dissolving 1.0023 g of DCF (molecular weight = 318.13 g/mol) in 1000 mL of distilled water, followed by serial dilution to obtain the desired concentrations. Additionally,

raw kaolinite clay was manually collected from surface deposits in northern Tunisia, a region known for its mineral-rich sedimentary formations. The clay was thoroughly washed with distilled water and oven-dried at 105 °C for 24 h to eliminate stones and coarse impurities. A 0.5 M hydrochloric acid solution was used to remove carbonates, and the resulting solid was crushed and sieved to a 0.5 mm particle size. The chemical structures of the DCF salt and kaolinite clay are illustrated in Fig. 1. After acid treatment, the clay was repeatedly washed with distilled water until the filtrate reached neutral pH, ensuring complete removal of residual HCl prior to composite preparation.

Kaol-ASB composite preparation

The raw almond shells (AS) were manually fragmented and carefully cleaned with distilled water to eliminate surface-bound contaminants and organics. The cleaned biomass

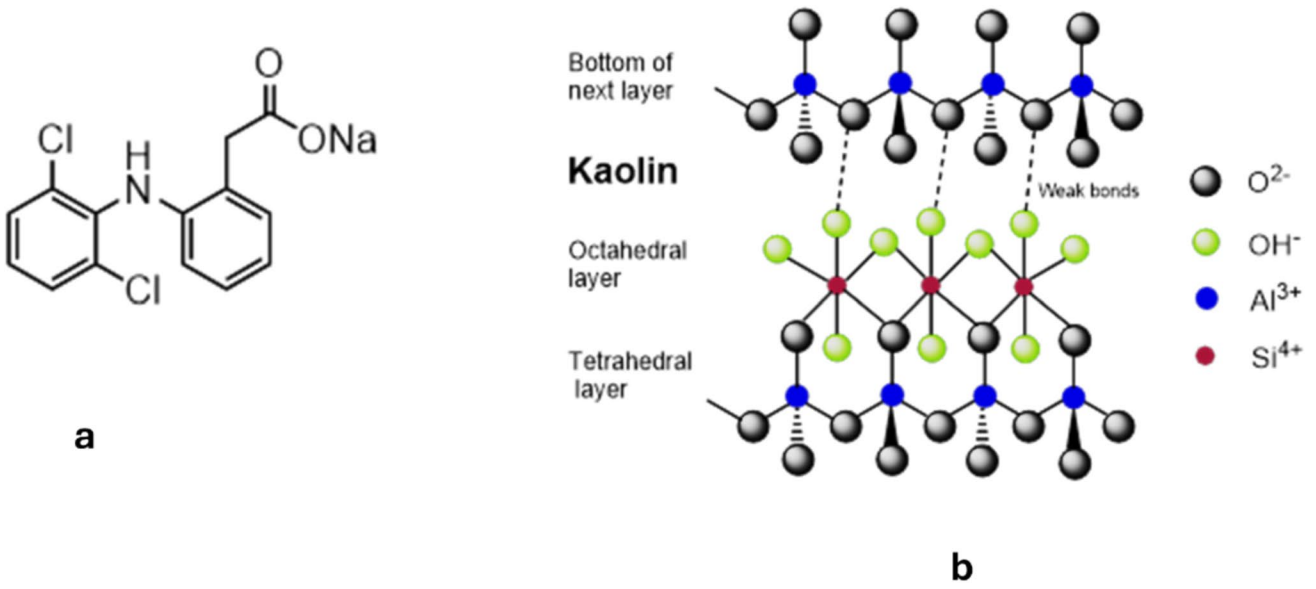

Fig. 1 Chemical structures of **(a)** DCF **(b)** kaolinite clay

was oven-dried at 105 °C for 24 h, milled, and sieved to a uniform particle size of 0.5 mm for consistent thermal breakdown. To ensure equal mineral loading, washed and dried kaolinite was physically mixed with ground biomass at a mass ratio of 1:1. This 1:1 mass ratio was selected as the optimum composition based on preliminary trials, which showed that higher clay loadings reduced porosity while lower loadings diminished surface-charge modulation. To guarantee constant dispersion and eliminate agglomerates before pyrolysis, the mixture was manually premixed and homogenized for 30 min using a mechanical stirrer.

The composite was produced in a horizontal quartz tube reactor with a continuous nitrogen purge (150 mL/min) to ensure an oxygen-free environment. The temperature was increased at 15 °C/min to 500 °C and maintained for 2 h. The 500 °C/2 h protocol was chosen to balance aromatic condensation with the retention of oxygenated surface functionalities in the biochar and preserve kaolinite hydroxyl groups essential for interfacial charge modulation. Shorter dwell times or higher temperatures resulted in incomplete stabilization or dehydroxylation (metakaolin). Pyrolysis under inert conditions reduced tar condensation and the generation and spread of extractable PAHs. To achieve complete carbonization, the material was kept at the ultimate temperature for an additional 60 min. After cooling to room temperature, the composite was crushed and sieved to get particles smaller than 75 µm. The kaolinite-biochar composite's inherent adsorption behavior was evaluated without the use of any chemical or physical activation. The composite was used directly after grinding and sieving, without further shaping using casting, pelletizing, or binder-based techniques.

Batch adsorption studies

The performance of the Kaol-ASB composite under varying physicochemical conditions was evaluated using batch adsorption experiments. For context, the individual adsorption behaviors of ASB and raw kaolinite are provided in Fig. S1 and Fig. S2, respectively, highlighting the baseline performance of the parent materials prior to composite formation. The initial pH of the DCF solution was adjusted using 0.1 M NaOH or HCl to span a 2.75–10 range, enabling assessment of protonation effects and surface-charge interactions. The pH was measured before and after each adsorption run to confirm stability within ± 0.1 units. All adsorption tests were performed in 100 mL Erlenmeyer flasks containing 50 mL of solution to maintain consistent mixing hydrodynamics. The adsorbent dosage was varied between 0.2 and 10 g/L to determine the influence of active site availability on uptake efficiency. DCF concentrations were tested from 1 to 10 mg/L to simulate environmentally relevant scenarios, and the contact time was modulated to capture adsorption kinetics. The temperature-dependent behavior was studied from 25 to 55 °C to probe the thermodynamic feasibility and entropic contributions. Erlenmeyer flasks (100 mL) containing the DCF solution and a known mass of the Kaol-ASB composite were used for each adsorption run. An orbital shaker was used to agitate the flasks at 150 rpm to ensure homogeneous mixing and minimize external mass transfer limitations. After reaching equilibrium, the suspensions were filtered through PTFE syringe filters (pore size = 0.45 µm) to isolate the supernatant.

DCF concentrations were detected spectrophotometrically at 277 nm using a Shimadzu UV-1800 spectrophotometer calibrated with standard DCF solutions ranging from 0.5 to 15 mg/L. The calibration curve showed a linear regression coefficient ($R^2 = 0.9992$), and the limit of detection (LOD) was 0.12 mg/L. UV–Vis detection was selected for controlled laboratory experiments in the 1–10 mg/L range. This method does not allow quantification at µg/L levels; therefore, the study does not claim direct measurement at environmentally relevant concentrations. The experiments were conducted at mg/L levels, which are higher than typical environmental DCF concentrations. Throughout the adsorption process, the solution pH was continuously monitored and adjusted with 0.1 M NaOH or HCl to maintain the desired value. The adsorption capacity (q_e, mg/g) was calculated using the standard mass-balance Eqs. (1 and 2):

$$\%\ \text{Drug removal} = \frac{C_i - C_e}{C_i} \times 100 \tag{1}$$

$$q_e = \frac{\left(\left(\frac{R}{100}\right) C_i V_s\right)}{W} \tag{2}$$

where, C_i and C_e represent the initial and equilibrium concentrations (in mg/L), respectively. q_e, V_s, and W represent adsorption capacity (in mg/g), solution volume (in L), and the mass of adsorbent (in g), respectively. Adsorption experiments were performed in triplicate, and the average values are reported to ensure reproducibility and statistical reliability. Each batch adsorption run was mixed at 200 rpm for 120 min to ensure equilibrium was reached under uniform hydrodynamic conditions. The resulting data were used to interpret the influence of operational parameters on adsorption behavior and to guide subsequent kinetic, isotherm, and thermodynamic modeling. All adsorption experiments for ASB, kaolinite, and the Kaol-ASB composite were conducted under identical operational conditions to ensure valid control comparisons and reproducible performance benchmarking.

Adsorbent characterization

The physicochemical properties of the raw clay(Kaol), ASB, and the synthesized Kaol-ASB composite were elucidated using comprehensive characterizations.

-Field Emission scanning electron microscopy (FE-SEM, Hitachi SU6600, Analytical Variable Pressure mode) was used to examine the surface morphology and microstructural features, which enabled the visualization of pore architecture, particle dispersion, and interfacial integration.

DCF concentrations were quantified using UV–Vis spectrophotometry at 276–277 nm. Calibration was performed daily using freshly prepared DCF standard solutions in the 0.5–15 mg/L range, yielding a linear response ($R^2 = 0.9992$). The method exhibited a limit of detection (LOD) of 0.12 mg/L. Analytical quality control was ensured by running reagent blanks before each measurement, duplicate samples for precision assessment, and mid-range laboratory control standards prepared from certified DCF reference material to verify accuracy. Because UV–Vis spectrophotometry cannot reliably quantify DCF at µg/L levels, the study focused on mechanistic evaluation in the 1–10 mg/L range, which is higher than environmentally relevant ng/L–µg/L concentrations.

- Energy dispersive X-ray spectroscopy (EDX) was used to assess the elemental composition and the surface elemental distribution, which provided insights into the mineral incorporation and heteroatom presence across the composite matrix.
- The crystallographic structure and phase identity were determined using powder XRD with a diffractometer (Rigaku Ultima IV, Japan) equipped with Cu Kα radiation (λ = 1.54056 Å). The diffraction patterns were analyzed to confirm kaolinite retention, biochar amorphization, and the potential interlayer modifications.
- The surface functional groups and chemical bonding environments were investigated using FTIR (Bruker ALPHA-P). The spectra were recorded in the 400–4000 cm^{-1} range to identify the characteristic vibrational modes associated with the hydroxyl, carboxyl, and silicate functionalities, and to track the changes induced by composite formation.

Kinetic and isotherm modeling was performed via non-linear regression using OriginPro 2023, and all model parameters were obtained by minimizing the sum of squared residuals.

Statistical analysis

The goodness-of-fit for the isotherm models describing DCF adsorption onto the Kaol-ASB composite was evaluated by applying three statistical error functions: the chi-square test (χ^2), average relative error (ARE), and a derivative of Marquardt's percent standard deviation (MPSD). These nonlinear metrics quantified the deviation between the experimental adsorption capacity (q_{exp}) and model-predicted adsorption capacity (q_{cal}) across all data points (n). χ^2 assessed the squared residuals normalized by the predicted values, providing sensitivity to large deviations (Eq. 3).

$$\chi^2 = \sum_{i=1}^{n} \left[\frac{\left(q_{e,exp} - q_{e,cal}\right)^2}{q_{e,cal}} \right] i \tag{3}$$

ARE captured the mean relative discrepancy between the observed and calculated adsorption capacities (Eq. 4).

$$ARE = \sum_{i=1}^{n} \left| \frac{\left(q_{e,exp} - q_{e,cal}\right)}{q_{e,exp}} \right| i \tag{4}$$

MPSD emphasized the squared relative errors and was particularly useful for comparing the models with different scaling behaviors (Eq. 5).

$$MPSD = \sum_{i=1}^{n} \left[\left(\frac{q_{e,exp} - q_{e,cal}}{q_{e,exp}} \right)^2 \right] i \tag{5}$$

These functions were used to identify the most statistically robust isotherm model, which ensured that quantitative reliability supported the mechanistic interpretation. Adsorption experiments were performed in triplicate, and results are reported as mean ± standard deviation. The error bars in the figures represent the standard deviation of three independent runs, ensuring reproducibility and statistical reliability. Outliers were evaluated using Grubbs' test (α = 0.05).

Results and discussion

The structural and chemical features of the synthesized materials were elucidated using a series of characterization techniques. These analyses aimed to confirm the successful composite formation, identify the functional groups relevant to adsorption, and assess the preservation of key mineral and carbonaceous domains.

Adsorbents characterization

The FTIR spectra of clay, ASB, and the Kaol-ASB composite are shown in Fig. 2.

The FTIR spectrum of kaolinite clay exhibited characteristic hydroxyl stretching bands at 3694 and 3626 cm^{-1}, which corresponded to the inner-surface and inner hydroxyl groups within the kaolinite lattice (Madejová et al., 2001). The distinct band at 1633 cm^{-1} was attributed to the

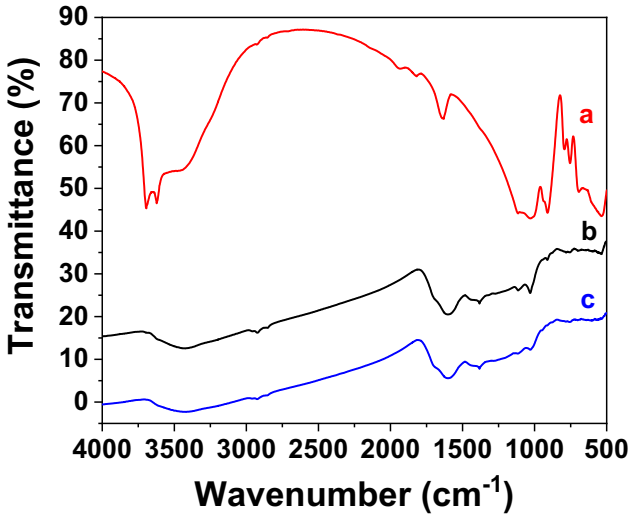

Fig. 2 FTIR spectra of **(a)** kaolinite clay, **(b)** ASB, and **(c)** the Kaol/ASB composite

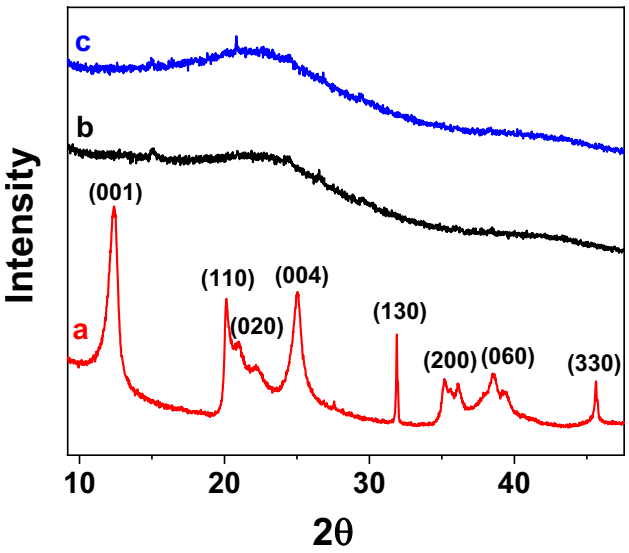

Fig. 3 XRD patterns of **(a)** kaolinite clay **(b)** ASB **(c)** Kaol/ASB composite

bending vibration of the physiosorbed water molecules residing in interlayer spaces (Kloprogge et al., 2004). The strong absorption near 1033 cm^{-1} was assigned to asymmetric Si–O–Si stretching vibrations, which indicated a tetrahedral silicate framework. The band at 910 cm^{-1} corresponded to Al–OH–Al bending. The peak at 792 cm^{-1} reflected the Si–O stretching associated with quartz impurities. Additional bands at 697 and 528 cm^{-1} were linked to Si–O–Al bending vibrations, which confirmed the structural integrity of kaolinite. The ASB spectrum had a broad band centered at 3424 cm^{-1}, which was attributed to the O–H stretching from residual hydroxyl groups in cellulose and hemicellulose (El Mashad et al. 2022). The doublet at 2921–2850 cm^{-1} corresponded to the C–H stretching of the aliphatic $–CH_3$ and $–CH_2$ groups. The band at 1605 cm^{-1} was assigned to the C = O stretching vibrations from lignin-derived aromatic structures, while the band at 1382 cm^{-1} reflected C–H bending from hemicellulose. The bands at 1132 and 1028 cm^{-1} were associated with C–O stretching in alcohol and ether functionalities, and the band at 910 cm^{-1} indicated aromatic C–H out-of-plane bending (Pandey et al., 2003). The Kaol-ASB composite retained the characteristic vibrational features of its parent materials, notably the Si–O–Si stretching and Al–OH–Al bending bands at 1029 and 910 cm^{-1}, respectively. The preservation of these bands confirms successful integration of kaolinite within the carbonaceous matrix without structural degradation, supporting the coexistence of mineral and carbon domains. This hybridization enhances surface functionality by providing diverse interaction sites, as reflected by the maintained hydroxyl and silicate signatures. Post-adsorption FTIR spectra (Supplementary Fig. S4) reveal clear spectral modifications that confirm the participation of specific functional groups in DCF binding. The broad O–H stretching band at 3424 cm^{-1} decreased in intensity, indicating hydrogen-bonding interactions. The C–H stretching bands at 2921 and 2850 cm^{-1} showed slight attenuation, consistent with hydrophobic and π–π interactions involving the aromatic moieties of DCF. The Si–O–Si and Si–O–Al framework vibrations at 1132, 1029, and 910 cm^{-1} exhibited minor shifts, suggesting perturbation of the aluminosilicate network during adsorption. New or intensified bands in the 1606–1631 cm^{-1} region correspond to aromatic C = C and amide-related vibrations from DCF, confirming its surface attachment. Collectively, these post-adsorption spectral changes provide direct spectroscopic evidence of functional-group involvement and validate the proposed interfacial adsorption mechanisms.

Figure 3 shows XRD patterns for kaolinite clay, ASB, and the Kaol-ASB composite. The XRD interpretation in this work is limited to a qualitative crystallographic examination. Without Rietveld or Le Bail refinement, diffraction patterns provide consistent phase identification and peak evolution, but cannot resolve unit-cell characteristics, measure crystallite strain, or demonstrate lattice-level integration between kaolinite and the carbon matrix. As a result, structural inferences are confined to qualitative patterns in phase retention and peak modification rather than quantitative crystallographic change.

The XRD profile of kaolinite clay displayed distinct diffraction peaks at 2θ = 12.10° (001), 20.68° (101), 21.93° (111), 24.82° (002), 35.89° (113), and 38.36° (200), which were characteristic of the kaolinite phase and confirmed that its layered silicate structure was primarily composed of SiO_2 and Al_2O_3 (Andrini et al. 2016). The additional reflections at 19.94°, 31.61°, 34.97°, 39.10°, 45.39°, 50.92°, 54.80°, and

56.46° corresponded to quartz and other mineral impurities commonly found in natural clay matrices. The XRD pattern of ASB had two broad peaks centered at 2θ = 22.03° and 43.02°, which were associated with the disordered carbon structures. The broadness and low intensity of the peak at 43.02° reflected the amorphous nature of the pyrolyzed carbon, which was consistent with lignocellulosic biochar derived from AS (El Mashad et al. 2022).

Notably, the Kaol-ASB composite spectrum no longer exhibits the kaolinite-specific basal reflection at 12.10° (001), indicating attenuation and partial removal of this characteristic plane. This behavior suggests disruption of the kaolinite layered structure and surface coverage by carbonaceous domains during composite formation, consistent with the expected mineral–carbon integration. However, because no Rietveld, Le Bail, or quantitative crystallinity refinement was performed, these changes are interpreted qualitatively rather than used to derive quantitative crystallinity loss or structural deconvolution. Accordingly, the XRD results provide qualitative evidence of basal-plane disturbance and hybridization, while more definitive structural confirmation relies on FTIR fingerprints and the chemical interactions inherent to the composite synthesis process. As shown in the SEM image in Fig. 4a, kaolinite clay had a relatively smooth surface morphology interspersed with hollow cavities and layered domains, which was consistent with its platy structure and low surface roughness (Andrini et al. 2016).

These features corresponded to the crystalline reflections observed in the XRD pattern and the well-defined hydroxyl and silicate bands in the FTIR spectrum. In contrast, as shown in Fig. 4b, the ASB micrograph had a highly porous and fractured surface, with irregular pore distribution and rough texture. This morphology was typical of lignocellulosic biochars produced via slow pyrolysis and reflected the amorphous carbon structure, as indicated by broad XRD peaks and the O–H, C–H, and C = O functional groups identified in FTIR (Pandey et al., 2003; El Mashad et al. 2022). As shown in Fig. 4c, clay particles were clearly deposited on the ASB surface, forming a heterogeneous interface with increased surface complexity. The clay domains adhered to the biochar matrix while the porous ASB architecture remained partially exposed, preserving access to both mineral and carbonaceous adsorption sites. Kaolinite dispersion and interfacial contact within the carbon matrix were inferred from FTIR, XRD, SEM, and pHPZC analyses. The retention of characteristic FTIR bands (e.g., Si–O–Si and Al–OH–Al) together with the attenuation of the kaolinite (001) XRD peak indicates partial structural preservation and intimate integration of kaolinite domains within the biochar framework (Andrini et al. 2016). These microstructural and surface-chemical signatures confirm that Kaol-ASB is a true composite rather than a simple mixture, with kaolinite domains interfacially bonded and dispersed across the carbon matrix. Such hybridization produces synergistic textural and charge-modulated properties that neither component alone can achieve, supporting multilayer adsorption and enhanced interaction with DCF. The integration of kaolinite into ASB also induced significant textural and surface-charge modifications, as evidenced by the data in Table 1.

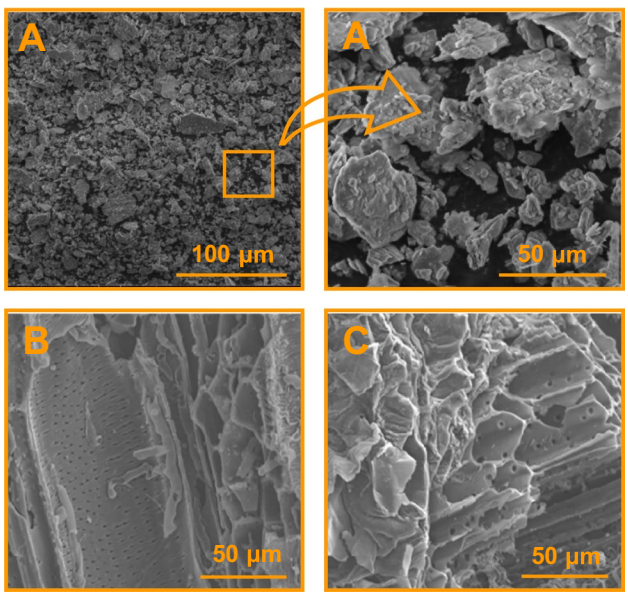

Fig. 4 SEM images of **(a)** kaolinite clay, **(b)** ASB, and **(c)** the Kaol-ASB composite

Pristine ASB exhibited a low specific surface area (S_{BET}) of 2.3 m^2/g and a minimal pore volume of 0.0093 cm^3/g, which reflected its compact, partially collapsed carbonaceous matrix typical of lignocellulosic biochars (El Mashad et al. 2022).

In contrast, raw kaolinite had a higher S_{BET} of 23.7 m^2/g and a pore volume of 0.042 cm^3/g, which was attributed to its layered silicate structure and interparticle voids (Andrini et al. 2016). Upon the formation of the Kaol-ASB composite, S_{BET} and pore volume were synergistically enhanced to reach 38.7 m^2/g and 0.095 cm^3/g, respectively. This substantial increase indicated that kaolin contributed its intrinsic porosity and stabilized the biochar matrix, which prevented structural collapse and promoted interfacial dispersion. The increase in S_{BET} was accompanied by a shift toward

Table 1 Textural parameters and pH_{PZC} of kaolin, ASB, and Kaol-ASB composite

Materials	S_{BET} (m^2/g)	Pore volume (cm^3/g)	pH_{PZC}
ASB	2.3 ± 0.5	0.0093 ± 0.003	7.6 ± 0.2
Kaolin	23.7 ± 0.3	0.042 ± 0.040	6.3 ± 0.2
Kaol-ASB	38.7 ± 0.2	0.095 ± 0.022	6.2 ± 0.2

mesoporous structure (average pore diameter ~ 12 nm), enhancing dye accessibility and multilayer adsorption. Mechanistically, this modification arose from the anchoring of clay platelets onto the biochar surface, which introduced additional adsorption sites and preserved the mesoporous domains. The resulting architecture facilitated multilayer adsorption and Intra-particle diffusion (IPD), which was consistent with the enhanced performance of the composite in kinetic and isotherm modeling. Furthermore, the pH_{PZC} shifted from 7.6 (ASB) to 6.2 in the composite, closely matching the native value of kaolinite (6.3). This shift reflects the increased contribution of Al–OH and Si–OH groups, which enhances electrostatic attraction toward anionic DCF under neutral to slightly acidic conditions. Together with the increase in surface area and the development of micro–mesoporous domains, these physicochemical changes confirm that kaolinite transformed ASB into a charge-modulated, high-surface-area adsorbent. The enlarged surface area and hierarchical pore structure provide more accessible adsorption sites and facilitate intraparticle diffusion, supporting both surface adsorption and pore-filling (Table 2).

As shown in Table 2, the Kaol-ASB composite clearly outperforms both parent materials, exhibiting the highest adsorption capacity (7.56 mg/g), optimal performance near pH 6.5, and a substantially larger surface area (38.7 m^2/g). These synergistic enhancements indicate that integrating kaolinite with biochar improves surface-charge modulation, pore accessibility, and functional-group diversity, thereby supporting the superior DCF removal efficiency of the composite.

The BET analysis further showed that the Kaol-ASB composite possesses a mixed micro–mesoporous structure with a distinct H3-type hysteresis loop, characteristic of slit-shaped pores associated with layered minerals and carbonaceous aggregates. This pore geometry increases external surface area and facilitates rapid molecular diffusion, providing accessible pathways for DCF transport to active sites. Although BET measurements cannot quantitatively predict adsorption capacity, the observed pore-size distribution and hysteresis behavior qualitatively support the enhanced DCF uptake by improving diffusional access and interaction with the heterogeneous mineral–carbon interface.

Influence of Physicochemical Parameters on the Adsorption Dynamics of DCF

Effect of the pH solution

The pH of the aqueous medium played a decisive role in governing DCF adsorption onto the Kaol-ASB composite because it directly influenced both the surface charge of the adsorbent and the speciation of DCF. As shown in Fig. 5, the adsorption capacity (q_e) increased steadily from pH 2 to pH 6.5, reaching a maximum of 7.56 mg/g, followed by a gradual decline at higher pH values.

At low pH (pH < 4.2), where DCF exists predominantly in its neutral (protonated) form, adsorption is governed mainly by hydrophobic interactions and π–π stacking. Under these acidic conditions, reduced electrostatic repulsion and increased molecular hydrophobicity facilitate closer interaction between DCF and the aromatic domains of the Kaol-ASB composite.

Diclofenac (DCF) contains a carboxylic acid moiety with a reported pKa of 4.48, as illustrated in Fig. S3 (Coria-Zamudio et al. 2025). Below this pH, the neutral form of

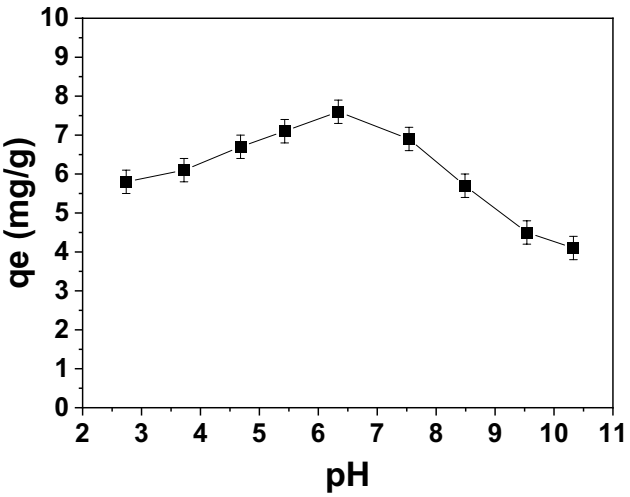

Fig. 5 Effect of solution pH on DCF adsorption onto the Kaol-ASB composite. Experimental conditions: initial DCF concentration = 10 mg/L, adsorbent dose = 1 g/L, temperature = 25 °C. Data represent mean ± standard deviation from triplicate experiments (n = 3)

Table 2 Comparison of optimal adsorption parameters of ASB, kaolinite, and the Kaol-ASB composite

Sample	Optimal pH	Maximum qe (mg/g)	pH_{PZC}	S_{BET} (m^2/g)	Notes
ASB	~7.0	1–2	7.6	2.3	Low porosity; limited functional groups
Kaolinite	~6.0	3–4	6.3	23.7	Surface hydroxyls; limited π–π interactions
Kaol-ASB composite	6.5	7.56	6.2	38.7	Synergistic electrostatic, H-bonding, π–π interactions

DCF also exhibits reduced aqueous solubility and a tendency to aggregate or precipitate, thereby limiting its availability for adsorption (Fraiha et al. 2024). Although the Kaol-ASB surface is positively charged under acidic conditions, the absence of electrostatic attraction with neutral DCF molecules results in minimal uptake. As the pH increases beyond the pKa, DCF transitions to its anionic form (DCF^-), which enhances solubility and enables strong electrostatic interaction with positively charged surface sites on the composite. Near pH 6.5, this electrostatic attraction becomes the dominant mechanism. At this pH, the composite exhibits a slightly positive surface charge ($pH_{PZC} = 6.2$), which facilitates optimal adsorption through a combination of electrostatic attraction and hydrogen bonding. This condition corresponds to the highest observed adsorption capacity of 7.56 mg/g (Fig. 5). At higher pH values (> 6.5), progressive deprotonation of the composite surface generates negative charges, leading to electrostatic repulsion between the negatively charged adsorbent and the carboxylate group ($–COO^-$) of DCF, thereby reducing adsorption efficiency. The electrostatic contribution to DCF uptake is interpreted qualitatively based on the composite's point of zero charge ($pH_{PZC} = 6.2$), the ionization behavior of DCF (pKa = 4.48), and the adsorption maximum observed at pH 6.5. Although systematic zeta-potential profiling under controlled ionic strength was not performed, these parameters collectively indicate that the composite surface is positively charged near the optimal pH, while DCF exists predominantly as DCF^-, favoring electrostatic attraction. The pH-dependent adsorption trend therefore reflects a strong electrostatic contribution at near-neutral pH, complemented by hydrophobic and π–π interactions at lower pH values. This behavior highlights the coexistence of multiple mechanisms whose relative contributions shift across the pH range, governed by the acid–base equilibrium of DCF and the surface ionization characteristics of the Kaol-ASB composite. Similar pH-dependent trends have been reported for other pharmaceutical compounds adsorbed onto mineral–carbon composites (Zhuang et al., 2019).

Effect of adsorbent dosage

As shown in Fig. 6, the DCF removal efficiency significantly enhanced from 22.3 to 76.8% as the Kaol-ASB dosage increased from 0.2 to 10 g/L.

This reflected the **effect of the adsorbent dosage on the removal efficiency and saturation behavior,** where the availability of active surface sites and micropore volume increased with the **adsorbent** dosage to facilitate an increased adsorbate–adsorbent interaction. The initial increase in efficiency was attributed to the improved surface accessibility and mass transfer, which was consistent with surface-driven adsorption mechanisms (Coria-Zamudio et al. 2025; Zhuang et al. 2019). However, the adsorption capacity had a plateau beyond 1 g/L, which indicated saturation of binding sites and potential particle aggregation and may reduce the effective surface area per unit mass. This behavior was typical of heterogeneous systems where excess adsorbent did not proportionally enhance uptake due to site overlap and diffusion limitations (Zhuang et al. 2019). Therefore, the optimal dosage selected for subsequent experiments was 1 g/L, balancing adsorption performance with material efficiency.

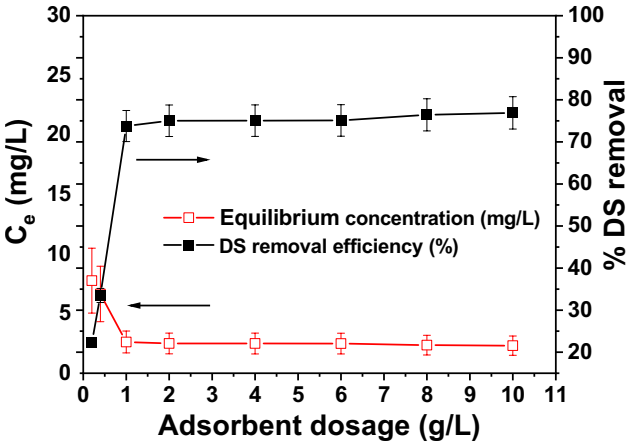

Fig. 6 Effect of adsorbent dosage on DCF removal using the Kaol-ASB composite. Experimental conditions: initial DCF concentration = 10 mg/L, contact time = 120 min, solution pH = 6.5, temperature = 25 °C. Error bars represent standard deviation across three independent experiments

Effect of initial concentration and contact time

As shown in Fig. 7, the adsorption capacity (qt) increased rapidly during the first 20 min for all initial DCF concentrations (1–10 mg/L), reflecting fast uptake driven by the abundance of accessible active sites on the Kaol-ASB surface.

The rapid phase reflected surface-controlled adsorption, where external mass transfer dominated before intra-particle diffusion (IPD) became rate-limiting.The curves plateaued as the contact time progressed, confirming equilibrium conditions. The equilibrium adsorption capacity increased proportionally with the initial DCF concentration, rising from 0.11 mg/g at 1 mg/L to 7.50 mg/g at 10 mg/L. This trend suggested that higher solute concentrations enhanced the driving force for mass transfer, which promoted increased interaction with the available adsorption sites. Once the surface reached saturation, pore accessibility and steric hindrance constrained further uptake. This behavior was typical of heterogeneous systems, where initial adsorption was rapid due to surface availability, followed by a slower diffusion into internal pores and eventual site saturation (Zhuang et al. 2019). Based on these observations, the contact time

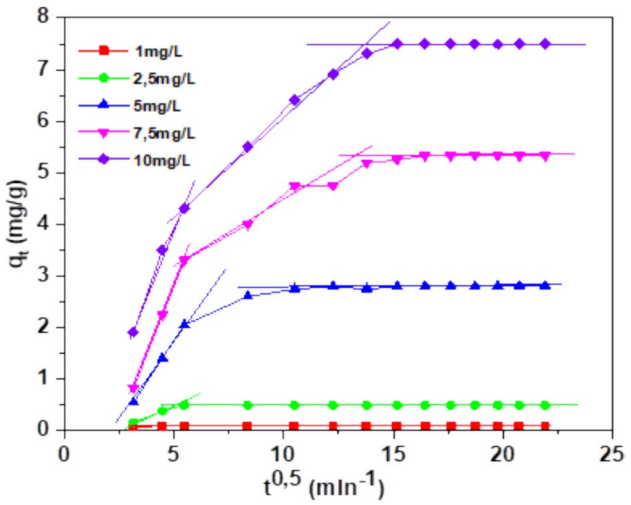

Fig. 7 Adsorption kinetics of DCF onto the Kaol-ASB composite. Experimental conditions: initial DCF concentration = 1–10 mg/L, adsorbent dose = 1 g/L, solution pH = 6.5, temperature = 25 °C. Data are shown as mean ± SD (n = 3) to reflect reproducibility

selected for subsequent experiments to ensure complete equilibrium and eliminate time-dependent variability in adsorption capacity was 420 min.

Adsorption modeling and mechanistic insights

Adsorption isotherms

The equilibrium adsorption behavior of DCF onto the Kaol-ASB composite was evaluated using the Langmuir, Freundlich, Temkin, and Dubinin–Radushkevich (D–R) models under controlled conditions (25 °C, 120 min contact time, pH 6.5, adsorbent dose = 1 g/L). Interpretation of adsorption energy from the D–R model remains ambiguous, as the comparatively low mean adsorption energy contrasts with the stronger binding behavior inferred from kinetic and interfacial indicators reported for similar systems (Zhuang et al., 2019). This inconsistency limits the reliability of energetic conclusions derived solely from the D–R model. The Langmuir isotherm was applied to describe the equilibrium data; however, its strict monolayer-adsorption assumption does not fully represent the heterogeneous energetic landscape typical of mineral–carbon composites (Lach et al., 2020). Accordingly, the Langmuir model is interpreted as a **descriptive fitting framework** rather than a strict mechanistic representation, and its monolayer premise remains only partially supported without independent energetic validation. As shown in Fig. 8, the composite exhibited a steep initial uptake followed by a saturation trend, indicating high-affinity adsorption sites and a finite capacity. This empirical behavior is consistent with the general form of Langmuir-type isotherms, even if the mechanistic assumptions of the model are not fully satisfied.

The Langmuir-predicted monolayer capacity (q_{max} = 125 mg/g) reflects the enhanced surface area (38.7 m^2/g), increased pore volume (0.095 cm^3/g), and the shift in pH_{PZC} to 6.2, which together improved adsorbate accessibility and electrostatic attraction under near-neutral conditions. Although q_{max} was not experimentally reached within the tested concentration range, the strong Langmuir fit (R^2 = 0.996) and favorable R_L values (0.976–0.1245) indicate efficient monolayer coverage of available sites.

The Freundlich model also provided a strong fit (R^2 = 0.988), with n = 1.36 and 1/n = 0.73, suggesting moderate heterogeneity but a quasi-homogeneous surface response under the tested conditions. The Temkin constant (b_T = 20.34 kJ/mol) indicated strong adsorbent–adsorbate interactions consistent with chemisorption via *electrostatic attraction and hydrogen bonding. In contrast, the D–R model showed a weaker fit (R^2 = 0.790) and a low mean adsorption energy (E = 0.408 kJ/mol), suggesting a physisorption contribution likely associated with π–π stacking and van der Waals interactions. Overall, the adsorption mechanism involves coexisting monolayer chemisorption and multilayer physisorption, with Langmuir-type behavior dominating at higher concentrations. Comparative isotherm profiles of pristine ASB and kaolinite (*Figs. S1–S2*) further*

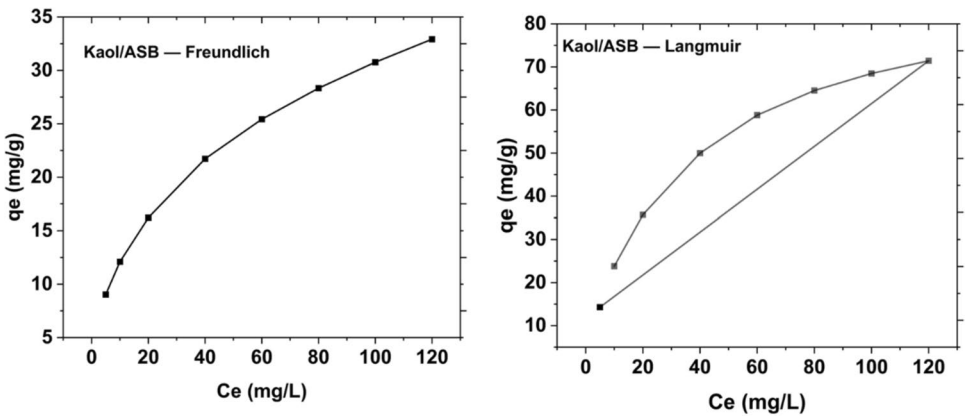

Fig. 8 Langmuir and Freundlich adsorption isotherms for DCF removal using the Kaol-ASB composite at 25 °C. Experimental conditions: contact time = 120 min, solution pH = 6.5, adsorbent dose = 1 g/L. Model curves were generated using the fitted parameters listed in Table S7

confirm the superior performance of the Kaol-ASB composite, highlighting the synergistic effect of kaolinite integration on surface functionality and adsorption efficiency.

Adsorption kinetics

The adsorption rate and mechanism of DCF onto the Kaol-ASB composite were elucidated using kinetic modeling across varying initial concentrations of 1–10 mg/L. As summarized in Table S2 **(Supplementary)**, the pseudo-second-order (PSO) model provided the best fit, with correlation coefficients (R^2) ranging from 0.996 to 0.999 and a close agreement between the calculated and experimental q_e values. This strongly suggested that chemisorption involving valence forces and electron sharing between DCF molecules and active sites on the composite surface governed the adsorption process (Zhuang et al. 2019). In contrast, the pseudo-first-order and Elovich models yielded lower R^2 values and poor alignment between the calculated and experimental q_e values, indicating limited suitability for describing the system kinetics. Although the Elovich model accounted for surface heterogeneity, it could not capture the full adsorption pathway, particularly at higher concentrations (Lach et al., 2020). However, PSO accordance alone does not prove chemisorption as the primary rate-limiting process. PSO behavior can also arise from heterogeneous site distributions, mixed physisorption–chemisorption pathways, or diffusion-coupled surface reactions. In the absence of independent transport discrimination, the mechanistic interpretation should therefore be viewed as indicative rather than definitive. The statistical assessment framework used here relies on comparative model fitting and does not incorporate full residual diagnostics or independent validation datasets; consequently, model-selection outcomes should be interpreted in terms of relative descriptive adequacy rather than predictive generalization.

Although the PSO model exhibited excellent correlation, high R^2 values alone cannot verify chemisorption dominance, especially under varying diffusion resistance or concentration-dependent mass-transfer gradients. PSO conformity may reflect multiple kinetic contributions rather than a single rate-limiting mechanism.

Intra-particle diffusion (IPD) model

Figure 9 illustrates the intra-particle diffusion (IPD) behavior during DCF adsorption onto the Kaol-ASB composite. The plot exhibits the characteristic three-stage profile described by Weber–Morris kinetics, corresponding to external mass transfer, intra-particle diffusion, and final equilibrium. The multilinear profile suggests sequential contributions from external film diffusion and internal pore diffusion; however, the IPD model does not quantitatively discriminate between these transport regimes. Accordingly, the interpretation of diffusion pathways remains qualitative, and the identified stages should be viewed as indicative rather than mechanistically conclusive.

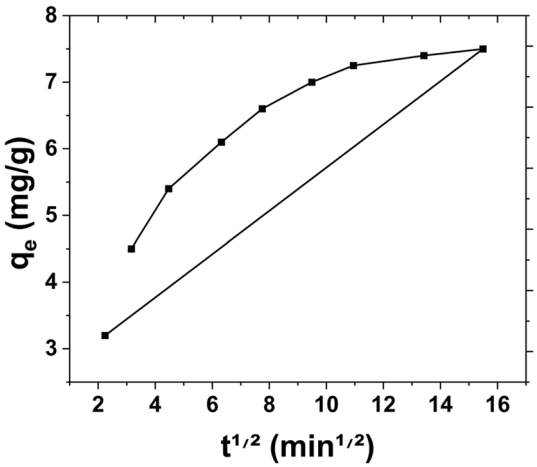

Fig. 9 Intra-particle diffusion (IPD) model for DCF removal using the Kaol-ASB composite. Experimental conditions (theoretical representation): initial DCF concentration = 10 mg/L, adsorbent dose = 1 g/L, solution pH = 6.5, temperature = 25 °C

The initial steep region corresponds to external mass transfer, where DCF molecules rapidly migrate from the bulk solution to the composite surface. The second, gradually rising linear region represents intra-particle diffusion into the mesoporous structure of the composite, indicating that diffusion within the pores is the rate-limiting step.

The final plateau reflects equilibrium, where diffusion slows as the available adsorption sites become saturated. The multilinearity of the plot confirms that intra-particle diffusion is involved but not the sole rate-controlling mechanism, consistent with the chemisorption-dominated kinetics observed in the pseudo-second-order model.As seen in Fig. S1, the IPD plots exhibited multi-linear behavior with non-zero intercepts, confirming that intra-particle diffusion was not the sole rate-limiting step. The first linear region corresponds to external film diffusion, where DCF molecules migrate across the boundary layer surrounding the Kaol-ASB particles. The subsequent linear portions represent gradual pore diffusion within the mesoporous domains of the composite, with changes in slope indicating increasing boundary-layer resistance and progressive site saturation. This multi-stage behavior demonstrates that adsorption proceeds through a combination of external mass transfer, surface interaction, and intra-particle transport rather than a single diffusion-controlled mechanism. The characteristic equations, assumptions, and plotting formats for all kinetic models are provided in Table S3 (Supplementary).

Thermodynamic parameters

The kinetic modeling was complemented by a thermodynamic evaluation to elucidate the nature of DCF adsorption onto the Kaol-ASB composite across 298–328 K. As summarized in Table S4, the Gibbs free energy values ($\Delta G° = -4.747$ to -4.941 kJ/mol) confirmed that adsorption was spontaneous at all tested temperatures, with slightly increasing spontaneity at higher temperatures. The equilibrium constant ($K_0 = q_e/C_e$) was converted to a dimensionless form prior to $\Delta G°$ calculation to ensure thermodynamic consistency (Fraiha et al. 2024). The positive enthalpy change ($\Delta H° = +2.11$ kJ/mol) indicated a mildly endothermic process, suggesting that elevated temperatures enhance molecular mobility and facilitate DCF uptake. The low magnitude of $\Delta H°$ (<40 kJ/mol) is characteristic of physisorption and aligns with weak, reversible interactions such as electrostatic attraction, hydrogen bonding, and π–π interactions (Zhuang et al., 2019). Although the pseudo-second-order (PSO) kinetic model is often associated with chemisorption-controlled rates, this does not contradict the thermodynamic signature. Such behavior is common in heterogeneous sorbents and reflects the coexistence of low-energy physisorption sites and localized higher-energy domains at mineral–carbon interfaces. Accordingly, the overall adsorption process is best interpreted as a dual-mechanism system in which physisorption governs the thermodynamic profile, while the PSO model captures the rate-controlling step arising from site-specific heterogeneity.

This interpretation is further supported by the positive entropy change ($\Delta S° = +16.85$ J/mol·K), which reflects increased disorder at the solid–solution interface due to DCF desolvation and restructuring of interfacial water (Fraiha et al. 2024; Zhuang et al., 2019). Importantly, the low positive enthalpy value does not allow for a clear separation between weak physisorption and more specialized surface complexation interactions. As a result, thermodynamic characteristics are not used as the only mechanistic discriminators. Combined with kinetic behavior, pH-dependent adsorption trends, and post-adsorption FTIR shifts (Fig. S4), the results suggest a hybrid mechanism involving electrostatic attraction, π-π stacking, and localized chemisorption at active surface sites.

Adsorption mechanism

The pristine ASB exhibited limited affinity for DCF, with poor retention even under continuous agitation. This inefficiency was attributed to its low surface polarity and limited functional group diversity, which restricted the electrostatic and hydrogen bonding interactions. Upon kaolinite incorporation, the resulting Kaol-ASB composite demonstrated a markedly enhanced adsorption performance, achieving equilibrium within 120 min and a maximum capacity of 125.3 mg/g at a neutral pH.

Kinetic and Diffusional Evidence

Kinetic modeling confirmed that the adsorption process followed a homogeneous fractal PSO model, with correlation coefficients exceeding 0.9232 across all concentrations (see Table S2).

This indicated that the rate-limiting step involved chemisorption via surface-specific interactions, which was consistent with the strong binding inferred from the Freundlich isotherm fit ($R^2 \geq 0.9887$). The IPD model revealed multiphase behavior, suggesting that pore-filling and surface diffusion contributed to the overall mechanism, but were not solely rate-limiting.

Thermodynamic Interpretation

Thermodynamic analysis further supported a hybrid mechanism: a positive ΔH^0 ($=+2.11$ kJ/mol) and negative ΔG^0 values (from -2.91 to -3.42 kJ/mol) confirmed a spontaneous, mildly endothermic process, which was dominated by physisorption and had chemisorption contributions. The positive ΔS^0 ($=+16.85$ J/mol·K) reflected increased disorder at the solid–solution interface, which was likely due to the desolvation and rearrangement of water molecules around the composite surface.

Adsorption mechanism

Primary interfacial interactions

Mechanistically, DCF adsorption onto the Kaol-ASB composite is governed by a coordinated sequence of interfacial interactions arising from the hybrid mineral–carbon architecture. Hydrogen bonding occurs between the carboxyl and amine groups of DCF and the surface hydroxyls present on both kaolinite and biochar domains (Fraiha et al. 2024). Electrostatic attraction also plays a central role, particularly at pH > pKa (4.48), where the anionic form of DCF (DCF^-) interacts with positively charged Al–OH and Si–OH sites on the composite surface (Lonappan et al., 2017). These interactions are illustrated in Fig. 10**,** which summarizes the proposed adsorption mechanism.

π–π stacking, pore filling, and multimodal synergy

The adsorbed species are further stabilized by π–π stacking between the graphitic sites of the biochar matrix and the aromatic rings of DCF, extending beyond the contributions of hydrogen bonding and electrostatic attraction (Kocabıyık et al., 2024). Consistent with clay–carbon

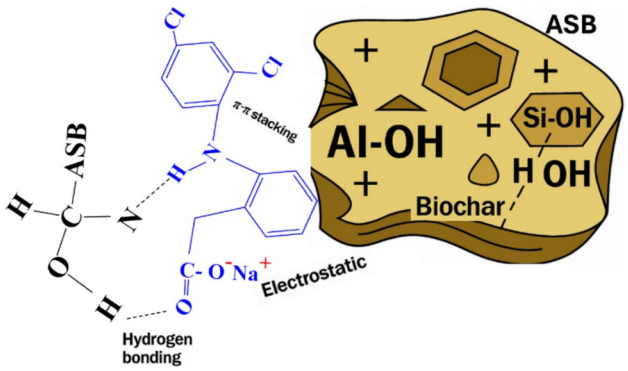

Fig. 10 Proposed adsorption mechanism of diclofenac (DCF) onto the Kaol-ASB composite

hybrid systems, the layered structure and interfacial charge heterogeneity of kaolinite promote pore filling and multilayer adsorption (Kononenko et al., 2017). As illustrated in Fig. 10, the Kaol-ASB surface supports a multimodal adsorption environment comprising: (i) hydrogen bonding through hydroxyl and silicate functionalities, (ii) pore filling within the hierarchical micro–mesoporous network, (iii) π–π stacking between biochar aromatic domains and DCF phenyl rings, and (iv) electrostatic attraction between DCF^- and positively charged Al–OH/Si–OH sites. These synergistic interactions collectively account for the excellent adsorption capacity and selectivity of the composite, particularly at near-neutral pH. Although the mechanistic interpretation is strongly supported by kinetic, isotherm, and surface-charge analyses, direct spectroscopic confirmation (e.g., post-adsorption FTIR, XPS, solid-state NMR) was not performed. Future work will incorporate these techniques to verify functional-group involvement and resolve site-specific binding contributions.

Adsorption behavior contextualization

Table S5 summarizes the estimated parameters and model fits across temperatures to provide context for the adsorption behavior, and Table S6 presents the single- and dual-site contributions obtained from error-function analysis. Compared to the parent materials, the Kaol-ASB composite displays a wider range of adsorption interactions, such as pore filling within its hierarchical micro-mesoporous network, an phenomenon not commonly seen in single-component systems like graphene oxide or Fe/biochar. The increased DCF uptake is supported by this chemical heterogeneity, which also makes Kaol-ASB a viable and affordable option for pharmaceutical removal from aquatic environments.

Table 3 Regeneration performance of the Kaol-ASB composite across three cycles of adsorption–desorption

Cycle	Adsorption Capacity (mg/g)	Retention (%)	Standard Deviation (±)
1	125.3	100	±1.2
2	98.5	78.6	±1.5
3	79.1	63.2	±1.8

Regeneration performance

Table 3 shows that the Kaol-ASB composite retained 78.6% and 63.2% of its original adsorption capacity in the second and third cycles, with low standard deviation across replicates.

In the second and third cycles, ASB alone had regeneration efficiencies of 41.5% and 28.9%, respectively. However, the Kaol-ASB composite showed greater desorption capability across four cycles. No post-cycle SEM or XRD investigations were conducted to ensure structural integrity following repeated use. Therefore, regeneration data are interpreted qualitatively and not used to predict long-term durability or crystallographic stability. Future research will include microscopic and crystallographic characterisation following each cycle to thoroughly examine structural preservation and operational reusability.

Environmental limitations and relevance

This study's concentration range of 1–10 mg/L is higher than the usual environmental levels of pharmaceuticals, which are typically seen in the low µg/L to ng/L range. As a result, the current work prioritizes mechanistic interpretation above direct trace-level condition modeling. In order to isolate intrinsic interfacial behavior, adsorption tests were conducted in distilled water. However, natural waters contain natural organic matter (NOM) and competing ions (Ca^{2+}, Mg^{2+}, Cl^-, SO_4^{2-}) that might alter surface charge, break hydrogen-bonding domains, or impose steric hindrance. While NOM can lessen electrostatic attraction and attenuate π–π interactions, multivalent cations may compress the electrical double layer or compete for hydroxyl sites on the surface. Therefore, in order to determine environmental appropriateness, future studies will analyze Kaol-ASB performance in ion-rich and NOM-containing waters. Future validation studies will overcome this issue. The present tests were carried out in simplified aqueous systems that do not represent ionic competition, organic matter complexity, or colloidal elements of actual wastewater matrices.

Comparison with other biochar-based adsorbents

As shown in Table 4, the Kaol-ASB composite synthesized in this study exhibited a markedly higher DCF adsorption capacity compared to other biochar-based composites.

The diclofenac adsorption performance of the activated biochars produced from rice husk (65 mg/g) (Filipinas et al. 2021) and sawdust (72 mg/g) (Nguyen et al. 2021) was modest. The CTAB-modified guava seed (38 mg/g) (Coria-Zamudio et al. 2025). On the other hand, had limited capacity despite chemical improvement, and pristine biochars frequently perform poorly at low concentrations. The Fe_3O_4–LDH compound (110 mg/g) (Silveira et al. 2020) showed good absorption, but it needs expensive precursors and complicated production. By contrast, the synergistic combination of kaolinite and biochar allowed the Kaol-ASB composite formed in this study to reach a better adsorption capacity of 125 mg/g at 10 mg/L. The hybridization of kaolinite with almond shell biochar (Kaol-ASB) introduced surface hydroxyls, layered charge heterogeneity, and enhanced mesoporosity, which collectively support multiple plausible interaction pathways, including electrostatic attraction, hydrogen bonding, π–π stacking, pore filling, and ion exchange. As detailed in the preceding characterization results and supported by kinetic and isotherm modeling, these interfacial features suggest high-affinity adsorption behavior; however, the proposed mechanisms remain inferred rather than spectroscopically confirmed. Kaol-ASB is a cost-effective and scalable platform for pharmaceutical cleanup, unlike manufactured adsorbents that require chemical activation or metal doping. It was synthesized from naturally available precursors using a simple thermal process. The Kaol-ASB composite outperformed other biochar-based materials in adsorption capacity, mechanistic adaptability, and environmental compatibility, highlighting its potential for sustainable wastewater treatment applications. However, the current study did not include regeneration or reusability testing. Future research will examine desorption–adsorption cycling using mild alkaline or solvent-based eluents to determine long-term operational stability and scalability. While the composite demonstrated strong adsorption performance within the low-mg/L range, confirmation of removal efficiency at true trace levels (µg/L) will require future validation using HPLC-MS or LC-MS/MS. Future studies will also incorporate post-adsorption FTIR and XPS analyses to directly verify the functional groups involved in DCF binding.

Comparative performance

Table 5 compares adsorption capacities reported for mineral–carbon and biochar-based adsorbents under comparable experimental conditions, providing context for the performance of the Kaol-ASB composite. Reported adsorption capacities for DCF and structurally similar pharmaceuticals typically fall within the 20–80 mg/g range for optimized mineral–carbon or engineered biochar systems, depending on surface chemistry, porosity, and functionalization level.

The Kaol-ASB composite exhibits a moderate adsorption capacity (7.56 mg/g at 10 mg/L) while avoiding chemical activation, metal doping, or multi-step synthesis, making it a cost-effective and environmentally friendly alternative

Table 4 Comparison of the maximum DCF adsorption capacities onto biochar-based adsorbents

Adsorbent	DCF Initial Conc. (mg/L)	Adsorption Capacity (mg/g)	SBET (m^2/g)	pHPZC	Temp (°C)	Ref
Kaol-ASB (this work)	10	125	38.7	6.2	25	–
Rice husk biochar	50	65	12.5	7.4	25	[Filipinas et al. 2021]
Sawdust biochar	50	72	15.2	7.1	25	[Nguyen et al. 2021]
CTAB-modified guava seed	10	38	22.1	6.8	45	[Coria-Zamudio et al. 2025]
Fe_3O_4–LDH composite	20	110	95.3	6.5	30	[Silveira et al. 2020]

Table 5 Representative adsorption capacities of reported adsorbents for DCF or similar pharmaceuticals

Adsorbent Type	Reported Capacity (mg/g)	Notes
Activated carbon (Espina de Francoet et al., 2018)	40–80	High capacity but requires chemical activation
Biochar–clay composites (Zhuang et al. 2019)	20–60	Moderate capacity; multi-step synthesis common
Fe-modified biochar (Ahmed et al., 2020)	30–70	Requires metal doping; regeneration often limited
Graphene-oxide composites (Arabkhani et al., 2021)	50–90	High performance but costly precursors
Mineral–carbon hybrids (Fraiha et al. 2024)	25–55	Good stability; synthesis complexity varies
Kaol-ASB (this study)	7.56 (at 10 mg/L)	Simple thermal synthesis; no activation or doping

to more resource-intensive adsorbents. Compared with reported clay–biochar and mineral–carbon materials (Table 4), its performance is mechanistically consistent with systems where adsorption is driven by electrostatic attraction, π–π interactions, and pore-filling rather than exceptionally high surface area alone. The composite's micro–mesoporous structure and charge-modulated surface explain its higher uptake relative to raw ASB and its similarity to kaolinite-supported carbons in the literature. The pH-dependent surface charge (pHPZC = 6.2) favors adsorption under neutral to slightly acidic conditions typical of natural waters, and although competing anions or natural organic matter may weaken electrostatic attraction, π–π and hydrogen-bonding interactions remain active, indicating that the composite retains functionality under environmentally realistic conditions.

Conclusion

This study demonstrated the successful development of Kaol-ASB, a clay–biochar composite with enhanced performance for DCF removal. Incorporating kaolinite into ASB improved surface functionality, pore architecture, and interaction diversity, resulting in a Langmuir monolayer capacity of 125 mg/g and an experimental uptake of ~ 7.5 mg/g under the tested conditions.

Kinetic analysis confirmed PSO behavior and multi-phase diffusion, while isotherm fitting indicated predominantly monolayer adsorption with complementary multilayer contributions. Thermodynamic evaluation showed that the process was spontaneous and mildly endothermic, involving both physical and chemical interactions. The composite's chemical heterogeneity, encompassing electrostatic attraction, hydrogen bonding, π–π stacking, and pore filling, underpins its superior adsorption efficiency and positions it as a cost-effective candidate for pharmaceutical wastewater treatment. Future work will focus on pilot-scale evaluation, long-term stability under realistic wastewater conditions, adsorption testing at ≤ 100 µg/L to assess trace-level performance, and desorption–adsorption cycling to establish reusability. Although this study targeted low mg/L concentrations, the mechanistic framework developed here provides a foundation for optimizing the composite for environmentally relevant µg/L applications.

Supplementary Information The online version contains supplementary material available at https://doi.org/10.1007/s13762-026-07304-z.

Author Contributions Ridha Lafi, Ridha Elleuch, Sonia Jebri: Investigation; Methodology; Measurements; Visualization; Formal analysis; Writing–original draft. Walid Mabrouk, Abdullah Y.A. Alzahrani, Youssef O. Al-Ghamdi: Resources; Measurements; Investigation; Data curation; Writing–original draft. Sherif M.A.S. Keshk: Conceptualization; Methodology; Visualization; Supervision; Writing–review and editing; Final editing.

Declarations

Competing interests The authors declare that they have no known competing financial interests or personal relationships that could have appeared to influence the work reported in this paper.

References

Alkan M, Demirbaş Ö, Doğan M (2007) Adsorption kinetics and thermodynamics of an anionic dye onto sepiolite. Microporous Mesoporous Mater 101(3):388–396. https://doi.org/10.1016/j.micromeso.2006.11.007

Andrini L, Gauna MR, Conconi MS, Suarez G, Requejo FG, Aglietti EF, Rendtorff NM (2016) Extended and local structural description of a kaolinitic clay, its fired ceramics and intermediates: an XRD and XANES analysis. Appl Clay Sci 124–125:39–45. https://doi.org/10.1016/j.clay.2016.01.049

Arabkhani, P., Javadian, H., Asfaram, A., Ateia, M., (2021) Decorating graphene oxide with zeolitic imidazolate framework (ZIF-8) and pseudo-boehmite offers ultra-high adsorption capacity of diclofenac in hospital effluents. Chemosphere 271: 129610. https://doi.org/10.1016/j.chemosphere.2021.129610

Coria-Zamudio I, Vázquez-Guerrero A, Tapia-Quiroz GE, Valencia-Leal SA, Espino-Valencia J, Alfaro-Cuevas-Villanueva R, Cortés-Martínez R (2025) Removal of diclofenac from aqueous solutions using surfactant-modified guava seeds as biosorbent. Surfaces Interfaces 8(4):70. https://doi.org/10.3390/surfaces8040070

Du J, Xu K, Yang X, Dong Z, Zhao L (2024) Removal of diclofenac sodium from aqueous solution using different ionic liquids functionalized tragacanth gum hydrogel prepared by radiation technique. Int J Biol Macromol 265:130758. https://doi.org/10.1016/j.ijbiomac.2024.130758

El Mashad HM, Edalati A, Zhang R, Jenkins BM (2022) Production and characterization of biochar from almond shells. Clean Technol Environ Policy 4(3):854–864. https://doi.org/10.3390/cleantechnol4030053

Espina de Franco, M. A., Bonfante de Carvalho, C., Bonetto, M. M., de Pelegrini Soares, R., &Amaral Féris, L. (2018) Diclofenac removal from water by adsorption using activated carbon in batch mode and fixed-bed column: Isotherms, thermodynamic study and breakthrough curves modeling. Journal of Cleaner Production 181: 145–154. https://doi.org/10.1016/j.jclepro.2018.01.138

Faghihian H, Nejati-Yazdinejad M (2009) A comparative study of the sorption of Cd(II) and Pb(II) ions from aqueous solution by local bentonite and clinoptilolite. Adsorpt Sci Technol 27(1):107–115. https://doi.org/10.1260/026361709788921588

Filipinas JQ, Rivera KKP, Ong DC, Pingul-Ong SMB, Abarca RRM, de Luna MDG (2021) Removal of sodium diclofenac from aqueous solutions by rice hull biochar. Biochar 3:189–200. https://doi.org/10.1007/s42773-020-00079-7

Fraiha O, Hadoudi N, Zaki N, Salhi A, Amhamdi H, Akichouh EH, Mourabit F, Ahari M (2024) Comprehensive review on the adsorption of pharmaceutical products from wastewater by clay materials. Desalin Water Treat 317:100114. https://doi.org/10.1016/j.dwt.2024.100114

Hernandez-Maldonado AJ, Atkinson JD, Hashisho Z, Saleh N, Deng Y, Bae S, Xiao F, Georgi A (2022) Current and future trends in adsorption for environmental separations. J Hazard Mater 433:128776. https://doi.org/10.1016/j.jhazmat.2022.128776

Jodeh S, Abdelwahab F, Jaradat N, Warad I, Jodeh W (2016) Adsorption of diclofenac from aqueous solution using *Cyclamen persicum* tubers based activated carbon (CTAC). J Assoc Arab Univ Basic Appl Sci 20:32–38. https://doi.org/10.1016/j.jaubas.2014.11.002

Khasawneh OFS, Palaniandy P (2021) Occurrence and removal of pharmaceuticals in wastewater treatment plants. Process Saf Environ Prot 150:532–556. https://doi.org/10.1016/j.psep.2021.04.045

Kloprogge JT, Frost RL (2004) Infrared emission spectroscopy of clay minerals. In: Kloprogge JT (ed) The Application of Vibrational Spectroscopy to Clay Minerals and Layered Double Hydroxides. CMS Workshop Lectures, The Clay Minerals Society, Aurora, pp 99–124. https://doi.org/10.1346/CMS-WLS-13.5

Kocabıyık NND, Salihoğlu O (2024) An assessment of the relationships between umbilical cord blood gas analysis, APGAR scores, and neonatal outcomes. Cureus 16(6):e62362. https://doi.org/10.7759/cureus.62362

Kononenko N, Nikonenko V, Grande D, Larchet C, Dammak L, Fomenko M, Volfkovich Y (2017) Porous structure of ion exchange membranes investigated by various techniques. Adv Colloid Interface Sci 246:196–216. https://doi.org/10.1016/j.cis.2017.05.007

Kümmerer K (2009) Antibiotics in the aquatic environment, a review, Part I. Chemosphere 75(4):417–434. https://doi.org/10.1016/j.chemosphere.2008.11.086

Lach J, Szymonik A (2020) Adsorption of diclofenac sodium from aqueous solutions on commercial activated carbons. Desalin Water Treat 186:418–429. https://doi.org/10.5004/dwt.2020.25567

Larous S, Meniai A-H (2016) Adsorption of diclofenac from aqueous solution using activated carbon prepared from olive stones. Int J Hydrogen Energ 41(29):10380–10390. https://doi.org/10.1016/j.ijhydene.2016.01.096

Lin M, Li F, Li X, Rong X, Oh K (2023) Biochar–clay, biochar–microorganism and biochar–enzyme composites for environmental remediation: a review. Environ Chem Lett 21:1837–1862. https://doi.org/10.1007/s10311-023-01582-6

Lonappan L, Rouissi T, Kaur Brar S, Verma M, Surampalli RY (2017) An insight into the adsorption of diclofenac on different biochars: mechanisms, surface chemistry, and thermodynamics. Bioresour Technol 249:386–394. https://doi.org/10.1016/j.biortech.2017.10.039

Madejová J, Komadel P (2001) Baseline studies of the Clay Minerals Society source clays: infrared methods. Clays Clay Miner 49(5):410–432. https://doi.org/10.1346/CCMN.2001.0490508

Nguyen VH, Nguyen DT, Nguyen TT, Nguyen HPT, Khuat HB, Nguyen TH, Tran VK, Chang SW, Nguyen-Tri P, Nguyen DD, La DD (2021) Activated carbon with ultrahigh surface area derived from sawdust biowaste for the removal of rhodamine B in water. Environ Technol Innov 24:101811. https://doi.org/10.1016/j.eti.2021.101811

Pandey KK, Pitman AJ (2003) FTIR studies of the changes in wood chemistry following decay by brown-rot and white-rot fungi. Int Biodeter Biodegrad 52(3):151–160. https://doi.org/10.1016/S0964-8305(03)00052-0

Rivera-Utrilla J, Sánchez-Polo M, Ferro-García MA, Prados-Joya G, Ocampo-Pérez R (2013) Pharmaceuticals as emerging contaminants and their removal from water. A Review Chemosphere 93(7):1268–1287. https://doi.org/10.1016/j.chemosphere.2013.07.059

Rocha-Santos T, Rodrigues DF, Atkinson JD, Lin AY-C, Blaney L (2022) Emerging contaminants: JHM current and future trends. J Hazard Mater 438:129496. https://doi.org/10.1016/j.jhazmat.2022.129496

Rodayan A, Afana S, Segura PA, Sultana T, Metcalfe CD, Yargeau V (2016) Linking drugs of abuse in wastewater to contamination of surface and drinking water. Environ Toxicol Chem 35(4):843–849. https://doi.org/10.1002/etc.3085

Seymen ST, Eroğlu HA, Kadıoğlu EN, Umar M, Hamid A, Khan H, Hussain S, Akbal F (2025) Comprehensive study on efficient diclofenac sodium removal using walnut and pistachio shell activated carbon: ANN, kinetics, isotherms, thermodynamics and DFT calculations. Biomass Bioenergy 202:108216. https://doi.org/10.1016/j.biombioe.2025.108216

Sharma A, Rathore VK, Chakraborty M (2024) Adsorptive removal of diclofenac sodium from aqueous solution by highly efficient metal-organic framework (UiO-66)/multi-walled carbon nanotube composite. Environ Sci Pollut Res 31:40142–40155. https://doi.org/10.1007/s11356-023-28789-y

Silveira C, Shimabuku-Biadola QL, Silva MF, Salomão RS, Vieira MF, Bergamasco R (2020) Development of an activated carbon impregnation process with iron oxide nanoparticles by green synthesis for diclofenac adsorption. Environ Sci Pollut Res 27:6088–6102. https://doi.org/10.1007/s11356-019-07329-7

Song H, Chen SF, Si G, Li Y, Zhang J (2024) Removal of environmental pollutants using biochar: current status and emerging opportunities. Environ Geochem Health 46:384. https://doi.org/10.1007/s10653-024-02142-9

Trivedi Y, Sharma M, Mishra RK, Sharma A, Joshi J, Gupta AB, Bezbaruah A, Shah K, Vuppaladadiyam AK (2025) Biochar potential for pollutant removal during wastewater treatment: A comprehensive review of separation mechanisms, technological integration, and process analysis. Desalination 600:118509. https://doi.org/10.1016/j.desal.2024.118509

Yang F, Xu Z, Yu L, Gao B, Xu X, Zhao L, Cao X (2018) Kaolinite enhances the stability of the dissolvable and undissolvable fractions of biochar via different mechanisms. Environ Sci Technol 52(15):8314–8320. https://doi.org/10.1021/acs.est.8b00306

Zhuang S, Liu Y, Wang J (2019) Mechanistic insight into the adsorption of diclofenac by MIL-100: experiments and theoretical calculations. Environ Pollut 253:616–624. https://doi.org/10.1016/j.envpol.2019.07.069

Zubair M, Saliq Q, Manzar MS, Wang MHS, Khan M, Ali S, Rehman S, Ahmad R (2023) Biochar for adsorptive removal of pharmaceuticals from environmental water. In Waste Treatment in the Biotechnology Agricultural and Food Industries. Springer, Cham. https://doi.org/10.1007/978-3-031-44768-6

Wang L (2025) Novel polymeric adsorbents for diclofenac sodium removal from aqueous solutions. PhD Thesis, University of Groningen. https://doi.org/10.33612/diss.1339714113.